Deposition of extended ordered ultrathin films of Au_38(SC_2H_4Ph)_24 nanocluster using Langmuir–Blodgett technique

Michal Swierczewski, Plinio Maroni, Alexis Chenneviere, Mohammad Dadras, Lay-theng Lee, Thomas Bürgi

Deposition of Extended Ordered Ultrathin Films of $Au_{38}(SC_2H_4Ph)_{24}$ Nanocluster using Langmuir–Blodgett Technique

Michal Swierczewski, Plinio Maroni, Alexis Chenneviere, Mohammad M. Dadras, Lay-Theng Lee, and Thomas Bürgi**

Langmuir–Blodgett technique is utilized to deposit ultrathin films of $Au_{38}(SC_2H_4Ph)_{24}$ nanocluster onto solid surfaces such as mica and silicon. The morphologies of the films transferred at various surface pressures within the mono/bi/trilayer regime are studied by atomic force microscopy (AFM). The time spent on the water surface before the deposition has a decisive effect on the final ordering of nanoclusters within the network and is studied by fast AFM, X-ray reflectivity, and grazing-incidence wide-angle X-ray scattering.

1. Introduction

Nanoscale particles attract a lot of attention due to their size-dependent optical,[1] electrical,[2,3] and chemical properties.[4,5] Of particular interest are ultrasmall metal nanoclusters (or clusters), which experience strong quantum confinement effect leading to profound changes in the atomic packing structure.[6,7] The synthesis of these atomically precise metal nanosystems, typically with metal cores smaller than 2 nm in diameter, makes use of stabilizing functional molecules, such as thiol ligands, hence deriving the common name—monolayer-protected clusters (MPCs).[8–10] The next stage toward applications, and at the same time a challenge in the field, is manipulation and controlled organization of MPCs into 2D superlattices, which would exhibit a collective response of the desired kind.[11,12] Multiple examples of deposition techniques have been extensively studied, including droplet evaporation,[13,14] spin-coating,[15] and chemical vapor deposition.[16] However, a common drawback of all these methods is the failure to form large-scale structures of closely packed particles.

There are several requirements necessary for successful formation of ordered self-assemblies of clusters.[17] The energy needed for migration of the molecules along the interface should be minimized in order to form dense structures. This is true when the interactions between the surface and the clusters (or their ligand shell) are identical at all point of the interface. At the same time, that interaction must be strong enough to allow the adsorption of the cluster from solution and fixation for further manipulation. Additionally, the surface must be completely flat. These conditions are challenging to fulfil using solid surfaces but are perfectly satisfied in the case of a Langmuir film, which is an ultrathin layer of particles adsorbed at a liquid–gas interface. This is typically achieved by spreading the solution containing the molecules of interest on the surface of water. The main advantage of this technique is the possibility to control the surface coverage by laterally compressing the films with movable barriers while monitoring the evolution of surface pressure–area (π–A) isotherms. As the total area available to the particles is reduced, the analysis of the curves' profiles may identify the formation of quasi 2D analogs corresponding to gaseous, liquid-expanded, liquid-condensed, and solid states, depending on the surface density.[18,19] Additionally, with the use of so-called Langmuir–Blodgett (LB) and Langmuir–Schaefer (LS) techniques, the films formed on the liquid–gas interface can be transferred to solid supports, largely expanding the range of analytical methods available for characterization, as well as satisfying the requirement for many potential applications.[20–22]

Historically, LB has been used for the study and transfer of long amphiphilic molecules such as carboxylic acids[23,24] or phospholipids,[25] whereby the hydrophilic part of the entity is anchored to the water surface and the hydrophobic parts face upward. Additionally, the stability of such monolayers can be aided by the reduction in surface energy as hydrogen bonds can be formed between the polar groups of the amphiphile and water molecules on the interface.[18]

When it comes to purely hydrophobic molecules, such as $Au_{38}(SC_2H_4Ph)_{24}$ cluster, much fewer reports of the formation of durable Langmuir films exist.[26–29] Typically, the stability of these monolayers requires the overall entropy of the system to rise as a result of adsorption of the particles on the air–water

M. Swierczewski, Dr. P. Maroni, Prof. T. Bürgi
Department of Physical Chemistry
University of Geneva
Geneva, 30 Quai Ernest-Ansermet, Geneva 4 CH-1211, Switzerland
E-mail: Thomas.Buergi@unige.ch

Dr. A. Chenneviere, Dr. L.-T. Lee
Laboratoire Léon Brillouin
UMR12 CEA-CNRS
Université Paris-Saclay
CEA-Saclay, Gif-sur-Yvette Cedex 91191, France
E-mail: Lay-Theng.Lee@cea.fr

Dr. M. M. Dadras
CSEM Centre Suisse d'Electronique et de Microtechnique SA
Neuchâtel 2002, Switzerland

The ORCID identification number(s) for the author(s) of this article can be found under https://doi.org/10.1002/smll.202005954.

DOI: 10.1002/smll.202005954

interface, for instance due to hydrophobic interactions between molecules.[18] In the case of long chain alkanes, such an increase in the disorder can be attributed to a higher degree of fluctuations allowed perpendicularly to the interface in comparison to the bulk state of the hydrocarbon.[30]

The relevant factors for $Au_{38}(SC_2H_4Ph)_{24}$ molecules include $\pi\cdots\pi$ and C—H$\cdots\pi$ interactions between phenyl rings of adjacent molecules,[31] which increase in strength with the degree of interdigitation between ligands of the cluster within the 2D assembly. For closed-shell metal centers that acquire an orientation that permits a close approach, metallophilic interactions may also be of importance.[32,33] Moreover, in the absence of stronger forces, van der Waals forces can have a significant contribution.[18] Nevertheless, the interactions between neighboring particles tend to be relatively weak for particles in the size range of 1–2 nm, which explains why only a few examples of LB films based on gold nanoclusters have been reported.[34–37]

Here, we study the formation and deposition of extended (mono)layers of $Au_{38}(SC_2H_4Ph)_{24}$ nanoclusters onto solid supports such as mica or Si by LB method. We utilize atomic force microscopy (AFM), high magnification transmission electron microscopy (TEM), X-ray reflectivity (XRR), and grazing-incidence wide-angle X-ray scattering (GIWAXS) to show that a degree of order is initially obtained between the particles. Temporal annealing successfully removes the mesoscopic defects between islands of nanoclusters but it does so at the cost of reducing the local order within the domains. To our knowledge, this is the first reported example of the deposition of ordered gold nanoparticles in such a small size regime.

2. Results and Discussion

The deposition of $Au_{38}(SC_2H_4Ph)_{24}$ onto mica using LB method was successful, as a dark gray shade was visible with the naked eye on the covered parts of the mineral sheet. The identity of the cluster in the film was confirmed by performing UV-vis transmission experiments of the film on mica and comparing to $Au_{38}(SC_2H_4Ph)_{24}$ cluster solution in dichloromethane (Figure S1, Supporting Information). Moreover, matrix-assisted laser desorption/ionization (MALDI) spectra were taken after using dichloromethane to rinse the cluster off the mica surface after LB transfer (Figure S2, Supporting Information).

2.1. LB Isotherms and Evolution of the Film Studied by AFM

A typical isotherm resulting from compression of $Au_{38}(SC_2H_4Ph)_{24}$ cluster on the air/water interface can be seen in **Figure 1**. The initial increase in surface pressure occurs at an area corresponding to ≈250 Å^2 per cluster molecule, which is followed by a smooth transition from gaseous to condensed state. The absence of any plateaus observed between states is the consequence of the complexity of the system, whereby multiple effects influence the compressibility curve.

A standard LB procedure requires the slope of the solid-state phase region of the isotherm to be extrapolated to the surface pressure of 0 mN m^{-1},[18] which is routinely performed to determine the coverage of the film and the packing of the molecules.

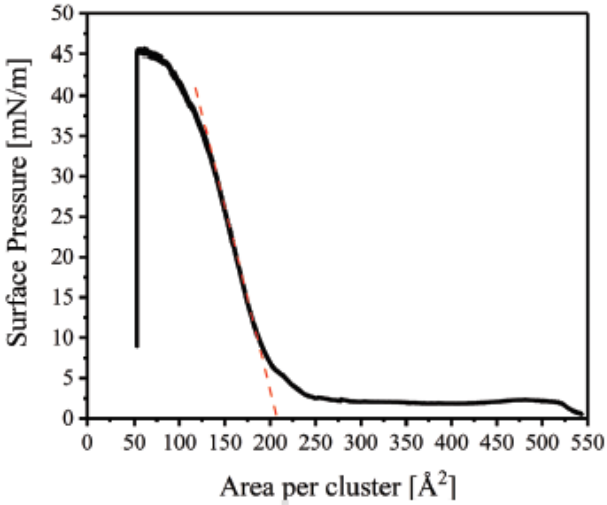

Figure 1. Surface pressure/area isotherm of $Au_{38}(SC_2H_4Ph)_{24}$ film. Dashed line determines the limiting critical area of the molecule at ≈205 Å^2.

Here, this limiting critical area is estimated to be ≈205 Å^2 (Figure 1). However, the calculation of the theoretical area of one $Au_{38}(SC_2H_4Ph)_{24}$ cluster molecule in a 2D lattice based on the crystal structure reported by Qian et al.[38] is not trivial. This is due to multiple possible orientations the prolate molecule can adopt on the surface, the degree of interdigitation of the ligands changing with surface pressure, as well as nonuniformity in 2D packing on the solid surface as evidenced in the fast AFM section (see below). The calculated values spread from 167 Å^2, in the case of vertical orientation, complete interdigitation of ligands and hexagonal close packed (hcp) structure, to 385 Å^2 if we assume horizontal orientation, extended ligands in a square close packed (scp) array (see the Supporting Information for calculations).

There is a large number of factors present in this complex system which can typically be associated with an increase in slope of the surface pressure isotherm. They include: changes in the orientation of the molecule,[39] shifts in phase of the lattice (degree of interdigitation between ligands),[18] and formation of multilayers of nonamphiphilic particles.[40] The overall transition from gaseous to condensed state is presumably a convolution of these effects.

Following the compression, if the films were held at a fixed area, their surface pressure dropped over time, indicating low stability of the monolayers. This is consistent with many LB studies of nonamphiphilic molecules that do not exhibit the stabilizing effect of hydrophilic and hydrophobic parts of the molecule directing the orientation on the water surface.[39,41] Weak van der Waals interactions stemming from the small size of the cluster can lead to facile buckling upward of the molecules and, hence, their build up in three dimensions.

Relaxation and subsequent recompression of the film resulted in steeper isotherms that began to rise at smaller areas, suggesting an increase in density of the cluster layer (Figure S3, Supporting Information). This can be primarily attributed to the aforementioned buckling up of clusters leading to formation of multilayers and aggregates, which do not separate upon relaxation of the barriers.

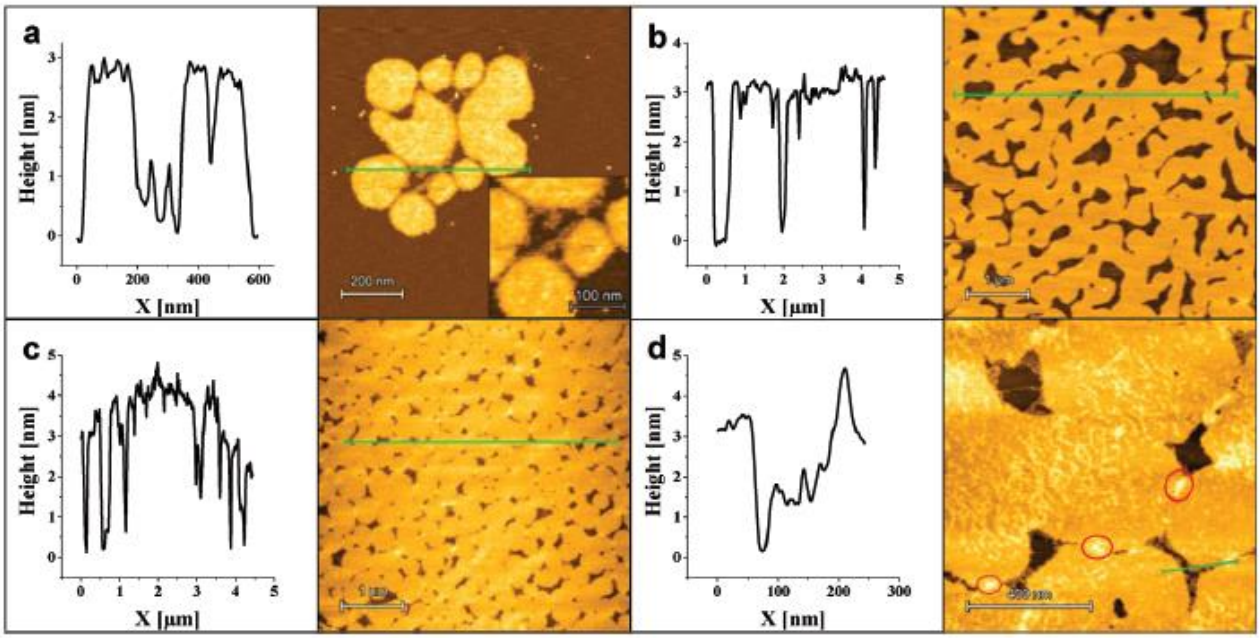

Figure 2. AFM images and corresponding height profiles of $Au_{38}(SC_2H_4Ph)_{24}$ films transferred onto mica: a) without compression or directly after reaching the target surface pressure of b) 9 mN m^{-1} and c,d) 18 mN m^{-1}.

The cluster films were deposited onto mica at selected points of the monolayer region of the isotherm directly after reaching the target surface pressure. **Figure 2** shows AFM images of films transferred a) without compressing the barriers, b) at 9 mN m^{-1}, and c,d) at 18 mN m^{-1}. Deposition of the uncompressed film results in a range of different morphologies inhomogenously distributed throughout the sample, more examples of which are shown in Figure S4 in the Supporting Information. Isolated groups of islands ≈100–400 nm in diameter are frequently formed, as seen in Figure 2a. The circular shape of the islands is a result of minimizing the Gibbs free energy of the system. Morphologies of this kind have been observed by multiple groups working on the deposition of larger nonamphiphilic particles by LB.[42,43]

The height output of AFM alone is not sufficient for the assignment of the number of layers but this issue has been resolved with the use of XRR (see below). However, a provisional assessment can be performed at this stage, while keeping in mind the uncertainty in orientation and degree of interdigitation of $Au_{38}(SC_2H_4Ph)_{24}$ molecules, as discussed earlier. Additionally, it has to be considered whether the molecules stack vertically on top of each other or the one on top falls in the gap between three neighboring molecules on the bottom (corresponding to AB stacking in hcp). The range of possible height values for a bilayer ranges from 2.75 nm, when the clusters are oriented horizontally on the surface, fully interdigitated and AB stacked, to 4.12 nm at the other extreme. The respective values for a trilayer are 3.63 and 6.18 nm (see the Supporting Information for calculations). These values can be compared to the step heights of the film measured in AFM and height analysis in XRR (see below).

Surprisingly, the film transferred without any compression exhibited a strong tendency to form films of height of around ≈2.8 nm, tentatively assigned as a bilayer. This is contrasted with the emergence of a thin monolayer stripe with a height of ≈1.4 nm at the contact point between two pancake-shaped bilayers, as seen in the inset of Figure 2a. Similar heights of 3.0–3.2 nm are observed for the film transferred at 9 mN m^{-1} (Figure 2b), in which compression of the barriers leads to the networks of islands of clusters being mechanically pushed closer together until they began to merge. As the surface pressure is increased, the diameter of the macroscopic islands does not vary considerably, as the shape observed before the compression can be discerned within the merged structure.

There is no evidence of a monolayer to bilayer transition in the π–A isotherm (Figure 1), typically exhibited as a plateau.[40] One possible scenario is that the formation of the bilayer, at least partially, takes place during the transfer onto mica, being induced by the drying and dewetting of the deposited film. This idea is supported by the TEM micrograph shown in **Figure 3**a, which shows the transfer of a $Au_{38}(SC_2H_4Ph)_{24}$ film at 5 mN m^{-1} onto a TEM grid using LB technique. The fact that the majority of the micrograph of the hydrophobic TEM grid is covered by a monolayer, whereas even at lower surface pressures bilayers are formed on hydrophilic mica (Figure 2a) strongly suggests that the transition is substrate dependent. The diameter of the clusters was measured to be 1.3 ± 0.2 nm, which is in very good agreement with the work of Wang et al.,[44] who used more advanced TEM techniques to observe Au_{38} clusters. At an increased surface pressure of 18 mN m^{-1}, bi/multilayers are detected in TEM (Figure 3b), which is justified by an increased apparent diameter of the clusters (1.9± 0.3 nm). This can be explained by some molecules being stacked on top of each other. Therefore, we conclude that the monolayer to multilayer transition presumably takes place partially on the water surface (as a result of compression) but also on the substrate

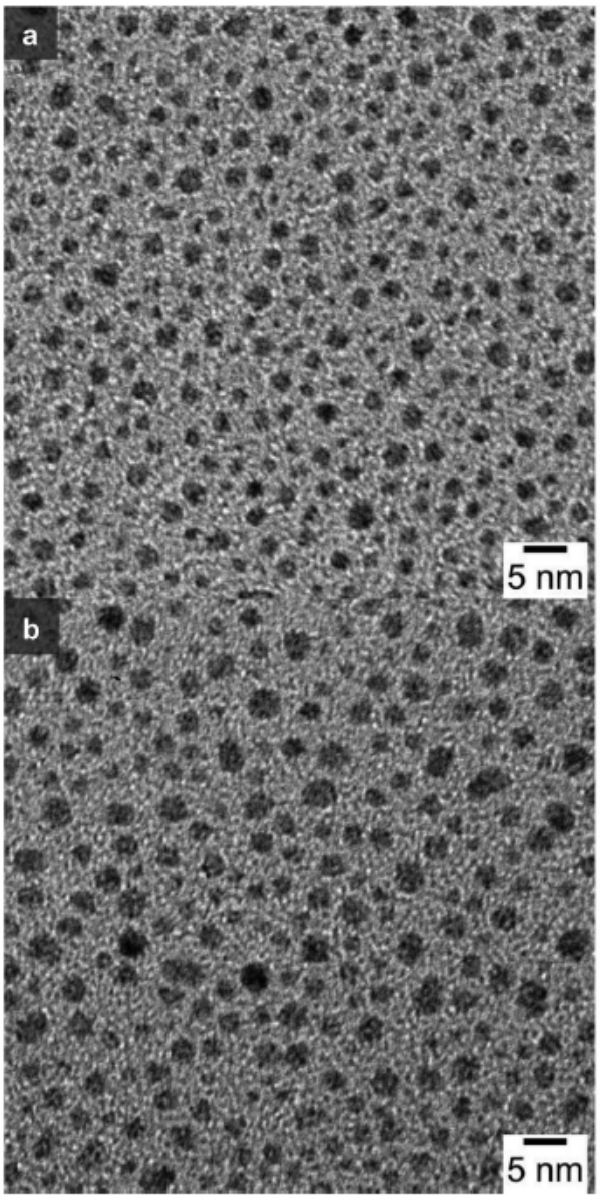

Figure 3. High magnification TEM micrographs of $Au_{38}(SC_2H_4Ph)_{24}$ film transferred onto a TEM grid using LB technique at a) 5 and b) 18 mN m^{-1}.

(as a result of drying/dewetting). It should be noted that the contribution of the less electron dense ligand shell toward the TEM signal is nonnegligible,[44] so the diameters obtained by TEM should not be directly compared to those found by XRR/GIWAXS, where we clearly identify the frontier between the core and the ligand (see below).

Interestingly, images in Figure 2a,b show that the film is composed of almost exclusively bilayers, suggesting that the transition is not random, as opposed to coexistence of mono, bi, and trilayers in the case of over-compressed film transferred at 18 mN m^{-1} (Figure 2c,d), which we describe in more detail later. Other groups working on LB experiments with larger gold or silver nanoparticles have similarly observed a strong preference of the film to form bi or trilayers.[45,46]

The majority of the area of the film transferred at 18 mN m^{-1} similarly exhibits heights within the bilayer range discussed above. However, inspection of Figure 2c,d shows that extra material is intermittently being deposited on top of the bilayer and measures up to ≈4.0–4.5 nm in height, which, by contrast with the bilayer, we tentatively classify as a trilayer. Further insight into the mechanism of merging of the islands can be speculated from Figure 2d. The additional third layer is randomly dispersed on top of the initial bilayer. However, the largest agglomerations of the extra material are predominantly localized on top of contact points, where islands had merged together upon compression (red circles in Figure 2d). Furthermore, the edges of the islands that are in close proximity to a contact point but do not quite touch another island often result in a monolayer. As a mechanism leading to the formation of this type of morphology, we suggest islands crashing into each other in a "tectonic" fashion, where in the central region of each pancake-shaped island there is material being buckled up and forming an additional layer. This is supported by an almost complete lack of such monolayers and trilayers of $Au_{38}(SC_2H_4Ph)_{24}$ in films transferred at surface pressures sufficiently low to prevent the originally formed bilayer islands to crash into each other due to significant lateral force, i.e., films seen in Figure 2a,b.

When the film is kept at a constant surface pressure for an extended period of time before the transfer, most of the defects that had appeared upon merging of the islands gradually disappear and the film becomes more homogenous on an extended scale. Films transferred onto mica, after having spent 3, 6, and 12 h on the water surface at a constant pressure of 18 mN m^{-1}, were examined by AFM as shown in **Figure 4**. Attention is drawn to the fact that the film continuously expands over lengths of at least tens of microns in each direction, which might be crucial for applications.

Maintaining constant surface pressure leads to drastic changes in morphology, which already manifest themselves after 3 h (Figure 4a), whereby the islands gradually disintegrate with time in order to cover the area available to them more effectively. This trend is sustained after 6 and 12 h (Figure 4b,c) as the coverage of the film increases and the size of gaps between islands diminishes with time the layer spends on water surface.

The gradual disappearance of the circular shape of the islands with time presents a feasible answer as to why the original bilayers shown in Figure 2 exhibited this morphology in the first place: the retained solvent likely controlled the curvature of the islands through interfacial tension, giving rise to a 2D bi-continuous phase as best seen in Figure 2b. When the film spent more time on the water surface, the solvent evaporated completely, which leads to spreading of clusters into the gaps previously formed between curved islands.

During long compression times, the area occupied by the film needs to be reduced considerably in order to keep the surface pressure constant. This is consistent with the aforementioned disappearance of the solvent retention effect but can also be reinforced by relaxation of the ligands and instability of the film. The additional compression leads to buckling up of the

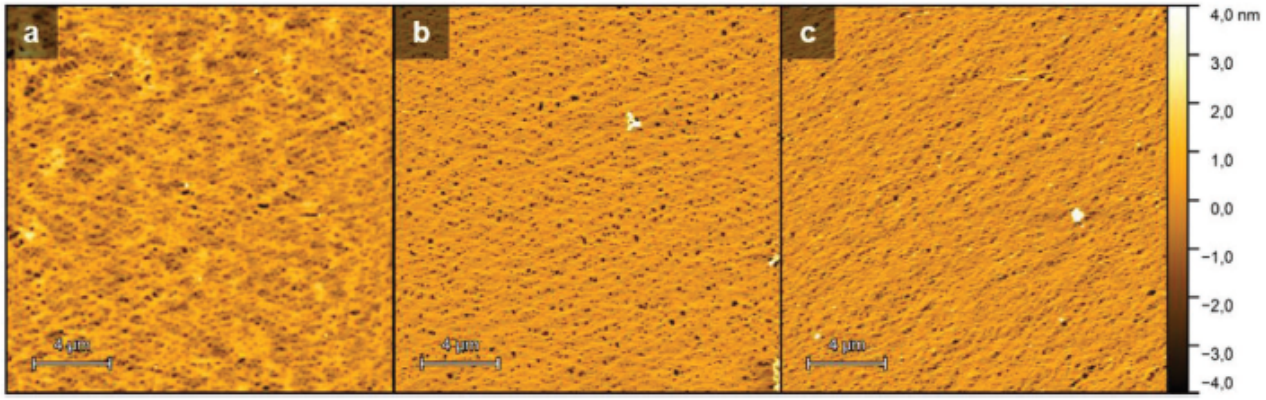

Figure 4. AFM images of $Au_{38}(SC_2H_4Ph)_{24}$ films transferred onto mica after being kept for a) 3, b) 6, and c) 12 h at a constant surface pressure of 18 mN m^{-1}.

molecules, resulting in heights of the films of ≈4–5 nm after being kept for 12 h at a constant pressure (relative to ≈3.5 nm at $t = 0$). Using AFM, we can solely speculate that this corresponds to a trilayer of $Au_{38}(SC_2H_4Ph)_{24}$ but XRR measurements confirm this conjecture (see below).

2.2. Investigation of the Local Order with Fast AFM

Fast AFM imaging in air was used to probe for local order between individual clusters as well as to image the molecules in higher resolution compared to conventional AFM. This was done for three $Au_{38}(SC_2H_4Ph)_{24}$ films deposited on silicon with varying amount of time spent on the water surface under constant compression before the transfer.

We consider two different AFM outputs of the same frame: height, which gives information about the topography of the outermost layer, shown in Figure S5 in the Supporting Information; and phase, which probes the mechanical properties of the film and is affected to various degrees by the top layer as well as the layers underneath, shown in **Figure 5**a–c and Figure S5 in the Supporting Information. The fact that the local order is notably easier detected in the phase output than in the height output of AFM suggests that the bottom layer(s) of the multilayered system are more ordered than the outermost layer(s), thus being manifested to a greater extent in the form of mechanical properties rather than as topographical features.

The highest degree of order was observed in the film deposited at 18 mN m^{-1} immediately after reaching the target surface pressure. Performing 2D fast Fourier transform (FFT) filtering on the phase output of AFM yields the image seen in Figure 5a, which facilitates the visualization of the hcp order. Presented as a 2D FFT shown in the inset, these data show increased intensity at the six vertices of a hexagon, from which a correlation distance of 1.7 nm can be extracted. However, one has to remember that the area considered here is on the order of tens of nm^2, so the GIWAXS measurements (see below) collected over an area of a few mm^2 should carry a much higher significance.

The film presented in Figure 5b was subjected to cyclic compression before the deposition at 18 mN m^{-1}. After reaching the target pressure for the first time, the barriers of the trough were fully relaxed and subsequently the film was compressed to the target pressure again. This cycle was performed four times in total before the transfer. After cyclic compression, the order changed from hcp to primarily scp with varying directionality. Although the correlation distance does not vary considerably from the one seen in Figure 5a, 2D FFT does not lead to a formation of any distinct pattern due to varying directionality of the scp in different parts of the image.

Fast AFM imaging of the film that spent 12 h on the water surface at constant pressure before transfer resulted in a markedly reduced degree of order being detected in comparison to the two films discussed above. Only very small ordered domains containing several $Au_{38}(SC_2H_4Ph)_{24}$ clusters were found as shown within red (hcp domains) and green (scp domains) circles in the 2D FFT-filtered image in Figure 5c. Additional imaging of a similar film aged for 12 h transferred onto mica at 16 mN m^{-1} was done with the use of fast AFM in liquid, which offers enhanced resolution but is less efficient at probing the order (Figure 5d). The measurement revealed that the clusters assemble themselves in small groups of molecules ranging in size from 10 to 20 nm, which equates to the size of domains of particles ordered in hcp or scp fashion detected by fast AFM in air (Figure 5c). This outcome is consistent with the investigation of Schultz et al. who concluded that larger gold nanoparticles similarly tend to form domains with the size equal to 5–6 lengths of the particles' diameter.[46]

Ultimately, one can conclude that, although annealing with time enhances the homogeneity of the Langmuir layer on a large scale and eliminates nearly all defects arising from the shape of the cluster islands merging together, this process happens at the expense of the local ordering between particles.

2.3. XRR and GIWAXS Measurements

Despite a degree of ordering being observed by fast AFM, our technique of choice for investigating order is XRR with the essential advantage being an immense increase in the studied area, whereby mm^2 rather than nm^2 are being considered. Specular reflectivity, which probes the vertical organization and GIWAXS, which gives information about the in-plane

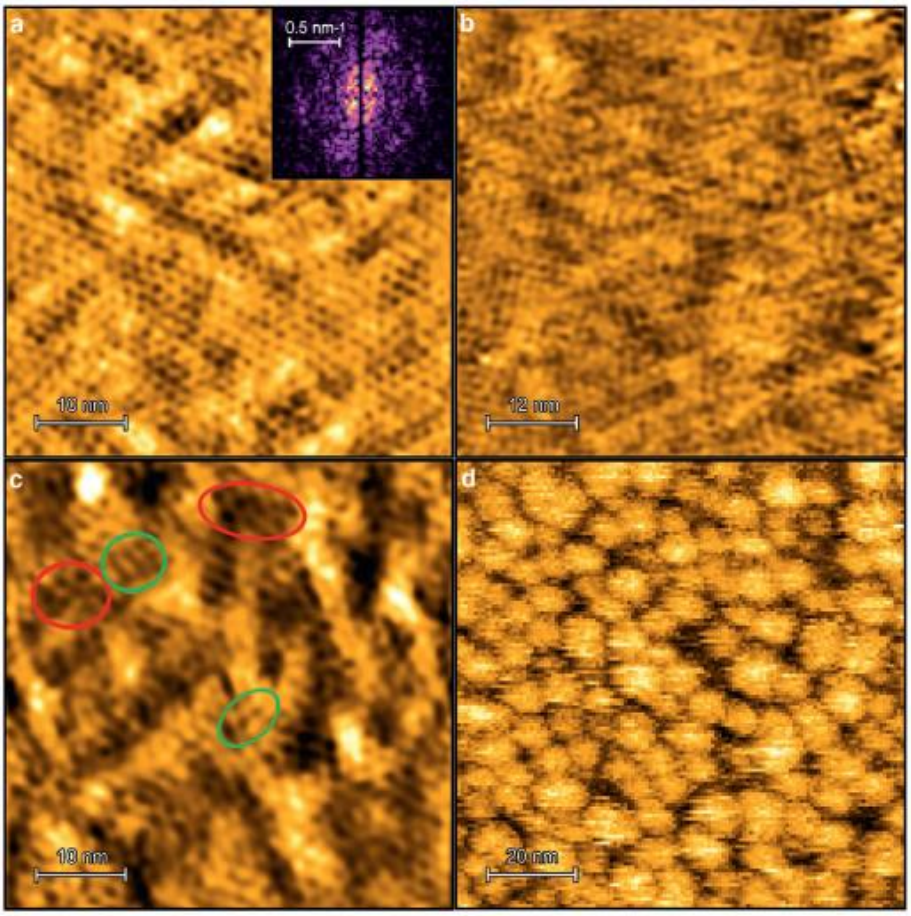

Figure 5. a–c) 2D FFT-filtered phase output of fast AFM images of $Au_{38}(SC_2H_4Ph)_{24}$ films transferred onto Si at 18 mN m^{-1} and measured in air: a) transfer at $t = 0$, 2D FFT shown in the inset, b) transfer after 6 h of cyclic compression following four cycles, c) transfer at $t = 12$ h; unfiltered images are shown in Figure S5 in the Supporting Information. d) Height output of unfiltered fast AFM image transferred onto mica at 16 mN m^{-1} at $t = 12$ h and measured in liquid.

correlation distance were employed. In conjunction with higher penetration depth than fast AFM (yet still very surface specific), XRR offers the possibility to observe ordering in semicrystalline samples that are investigated in this study.

In this set of experiments, we compare two films transferred onto mica after 12 h spent on water surface, where the method of compression of the barriers is modified. In the first scenario, the aim was to maintain a constant pressure of 18 mN m^{-1} for the duration of the annealing time. The second film was formed by initially compressing the barriers at a rate of 1 mm^2 min^{-1} to the same area as the final area of the first film. Subsequently, the barriers were kept constant at this area for 12 h before the transfer. XRR was used to elucidate the differences between these two compression methods. The reflectivity curves of both films are shown in **Figure 6**. The corresponding AFM images are included in Figure S6 in the Supporting Information.

The reflectivity curve for the film kept at constant pressure shows interference fringes that indicate a very well-defined transferred layer. The spacing between the local minima, $\Delta Q = 2\pi/h = 0.112$ Å^{-1}, gives a model-independent overall thickness, $h = 5.59$ nm. The small peak at $Q_z = 0.31$ Å^{-1} comes from the mica, also observed on the pure mica curve (Figure S7, Supporting Information). Curve-fitting of the reflectivity curve reveals a very well-organized internal multilayer structure. The fitted scattering length density profile (SLD, shown in the inset) shows three distinct maxima, which can be interpreted as layers rich in gold core of $Au_{38}(SC_2H_4Ph)_{24}$ (high in electron density), separated by low electron density organic ligands of the cluster. Here, $z = \infty$ is the bulk substrate and $z = 0$ is the air/film interface. The thicknesses of the three gold-rich layers are 1.14, 1.17, and 1.18 ± 0.02 nm intercalated by ligand layers of 0.5–0.6 ± 0.02 nm. The low-density layer next to the mica substrate, which can vary from 1.1 to 1.5 nm between substrates, is identified as a hydration layer, which is also present in the curve for pure mica (Figure S7, Supporting Information).

The film kept at constant area was initially compressed to the final area resulting in maximum surface pressure of 35 mN m^{-1} and then allowed to relax at constant area for 12 h. During this relaxation, the surface pressure gradually dropped to 10 mN m^{-1}. Pre-analysis with AFM showed that both films exhibit similar coverage, height, and topography (Figure S6, Supporting Information). However, the reflectivity curve in

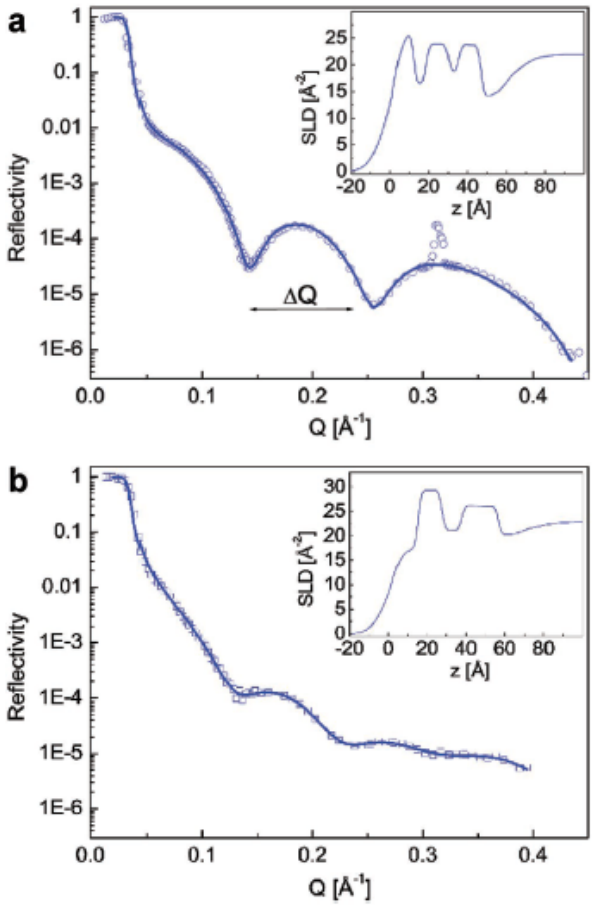

Figure 6. XRR curves of $Au_{38}(SC_2H_4Ph)_{24}$ films transferred onto mica after 12 h with varying barrier control mechanism: a) kept at constant surface pressure of 18 mN m^{-1}; b) kept at constant area identical to final area of sample (a). Insets show the corresponding data fitted to a multi-layered model. SLD is scattering length density (in 10^{-6} $Å^{-2}$). High and low electron density profiles correspond to gold cores of the clusters and ligands, respectively. $z = \infty$ is the bulk substrate and $z = 0$ is the air/film interface.

Figure 6b proves that the internal structure of the film, for which the area was maintained constant, was considerably less well-defined. The internal structure shows two gold-rich layers of uneven thicknesses, 1.23 and 1.89 ± 0.02 nm separated by a low electron density region of 1.01 ± 0.02 nm, and a large gold-poor region spanning 1.49 ± 0.02 nm at the air interface. These results suggest that the over-compression in the initial part of the experiment leads to wrinkling and creation of disorder between the layers.

Although the vertical composition of the two films is very different, their horizontal organization obtained from GIWAXS experiments is almost identical, as seen in **Figure 7**a and Figure S8 in the Supporting Information. Both films show amorphous peaks at 0.38 and 0.39 $Å^{-1}$, which correspond to a correlation distance of 1.65 and 1.63 ± 0.02 nm for compression controlled by area and surface pressure, respectively. The almost perfect alignment of the in-plane structure peak identified in GIWAXS is represented in the line intensity cut near the Yoneda peak at the near-total reflection edge of the specular reflection, Q_z = 0.025 $Å^{-1}$ shown in Figure 7b. The fact that both samples exhibit almost the same amorphous peak supports the claim that the order and the correlation distance are introduced early in the process of LB compression, as reported in the past for larger gold nanoparticles.[35] Fast AFM evidenced that temporal annealing leads to a decrease in order within the domains, as well as reduction in directionality between them. However, from XRR measurements it appears that, even though the vertical organization drastically depends on the mode of compression, the correlation distance within the domains remains unchanged.

Combination of the specular reflectivity XRR and GIWAXS data yields valuable information about the interdigitation of ligands between cluster molecules. Based on Figure 6a and 7a, it was shown that the average gold core size is 1.16 nm and the average interparticle core to core distance is 1.64 nm. It follows that the average experimental length of two ligands between neighboring clusters is 0.48 nm. The calculated value with no interdigitation is 0.84 nm in the vertical direction and 0.96 nm in the horizontal direction. It should be noted that there is a possible electron density contribution from cluster polydispersity and gold cores detected at different z values toward the local minima corresponding to ligand layers, which might decrease their apparent thickness. Therefore, it can be concluded that the degree of interdigitation accounts for a reduction of the ligand bilayer length up to 43% if the clusters are oriented vertically and up to 50% for horizontal orientation of the clusters in the case of AA stacking.

AB stacking adds more electron density to the z region of gold cores, as they are brought closer together in height, which would decrease the thickness of the ligand layers in the SLD plot. Therefore, in AB stacking the reduction of ligand thickness originating from interdigitation is smaller than in the case of AA stacking, but the precise values are complex to calculate as the extent to which gold cores are brought closer together in height strictly depends on the degree of interdigitation, creating a system with two unknown interdependent values (see the Supporting Information).

3. Conclusion

LB technique has been utilized to transfer ultrathin films of $Au_{38}(SC_2H_4Ph)_{24}$ nanocluster onto a number of solid supports, which is required for the analysis and future applications. AFM imaging of films transferred onto mica at gradually increasing surface pressures and following various lengths of time spent on the water surface under constant compression before the deposition laid ground for the proposal of formation of the observed morphology. The Gibbs free energy of the mesoscopic nanocluster islands is initially minimized by adopting a disk-like shape due to the presence of the retained solvent, an effect which diminishes with time. Fast AFM imaging showed that an extended hcp order can be observed in films transferred onto silicon following a short compression time, whereas longer compression results in disorganization and emergence of mixed hcp/scp ordering confined to small domains. The vertical and in-plane organization of $Au_{38}(SC_2H_4Ph)_{24}$ clusters

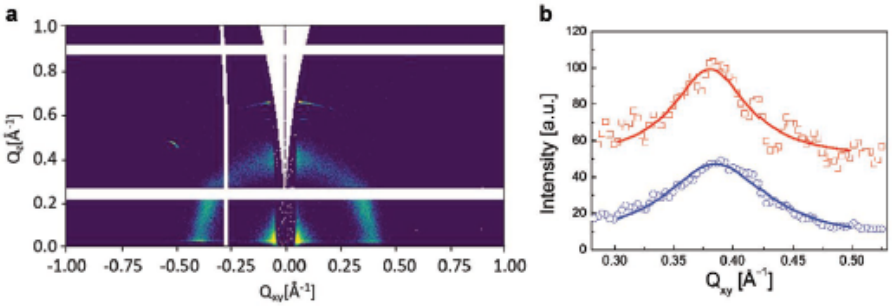

Figure 7. a) GIWAXS of $Au_{38}(SC_2H_4Ph)_{24}$ film transferred onto mica after 12 h of being kept at constant surface pressure of 18 mN m^{-1}; b) line intensity cut near the Yoneda peak at $Q_z \approx 0.025$ Å^{-1} for (a) (blue, bottom) and for film kept at constant area for 12 h before the transfer (red, top, GIWAXS shown in Figure S8, Supporting Information). Peaks at 0.38 and 0.39 Å^{-1} correspond to a correlation distance of 1.65 and 1.63 nm; the solid lines are Lorentzian fits to the correlation peaks.

within the film as well as the degree of interdigitation between the ligands of neighboring molecules has been studied with the use of XRR and GIWAXS. This combination of analytical tools shows that LB can be a suitable method for the deposition of extended ordered films of atypical LB molecules, such as non-amphiphilic gold nanoclusters in the very small size regime of 1–2 nm.

4. Experimental Section

Chemicals: Tetrachloroauric(III) acid trihydrate ($HAuCl_4{\cdot}3H_2O$, 99.99%, Aldrich), 2-phenylethanethiol ($Ph_2C_2H_4SH$, 99%, Aldrich), *L*-glutathione (GSH, 98%, Acros Organics), sodium borohydride ($NaBH_4$, 99.99%, Aldrich), acetone (99.9%, Fisher), tetrabutylammonium hexafluorophosphate ($TBAPF_6$) (98%, Fluka), toluene (99.8%, Fisher), ethanol (99.8% Fisher), methanol (99.9%, Fisher), dichloromethane (HPLC grade, 99%, Carl Roth), *n*-hexane (HPLC grade, 97%, VWR), and chloroform (99.8%, Fisher) were used as received.

Synthesis and Isolation of Monodisperse rac-$Au_{38}(SC_2H_4Ph)_{24}$: Racemic $Au_{38}(SC_2H_4Ph)_{24}$ nanocluster was prepared according to the previously reported procedure.[47] Briefly, tetrachloroauric acid trihydrate (1 g, 2.54 mmol) and *L*-glutathione powder (3.1 g, 10.18 mmol) were co-dissolved in acetone (100 mL) under vigorous stirring for ≈20 min at room temperature. After cooling the yellow suspension in an ice bath to ≈0 °C for ≈20 min, a solution of sodium borohydride (0.96 g, 25 mmol) in pre-cooled Milli-Q water (30 mL, resistivity 18.2 MΩ cm) was quickly added under vigorous stirring. Formation of Au nanoclusters was indicated by rapid change of the solution to black. After ≈20 min, the clear acetone was decanted and Milli-Q water (30 mL) was added to dissolve the glutathione-protected Au_n nanoclusters ($Au_n(SG)_m$). Ethanol (1.6 mL), toluene (10 mL), and 2-phenylethanethiol (10 mL) were added to the $Au_n(SG)_m$ and the mixture was heated at 80 °C for ≈24 h under air atmosphere. During the long time etching process, the polydisperse Au_n nanoclusters were converted to $Au_{38}(SC_2H_4Ph)_{24}$ clusters. Excess thiol was removed by washing thoroughly with methanol. $Au_{38}(SC_2H_4Ph)_{24}$ nanocluster was extracted from the mixture with Au(I)-SG by dichloromethane or toluene. Polydisperse $Au_{38}(SC_2H_4Ph)_{24}$ clusters were passed through a size-exclusion chromatography column packed with Bio-Rad BioBeads SX-1 with toluene as a mobile phase. The collected fractions were characterized by UV-vis spectroscopy, until no further change was observed. The resulting monodisperse $Au_{38}(SC_2H_4Ph)_{24}$ nanoclusters were characterized with UV-vis spectroscopy and MALDI mass spectrometry. UV-vis spectra of the clusters in solution were measured in toluene on a Varian Cary 50 spectrophotometer using a quartz cuvette of 1 cm path length. UV-vis spectra of films on mica were measured using JASCO V-670 spectrophotometer with ARSN-733 absolute reflectance manual stage; angle of incidence = 0° (transmission mode). MALDI spectra were collected using a Bruker Autoflex mass spectrometer equipped with a nitrogen laser at near threshold laser fluence in positive linear mode. [3-(4-*tert*-Butylphenyl)-2-methyl-2-propenylidene] malononitrile (DCTB) was used as the matrix with a 1:10, 1:100, and 1:1000 analyte:matrix ratio. A volume of 2 µL of the analyte/matrix mixture was applied to the target and air-dried.

Deposition on Solid Substrates using LB Technique: Before starting the experiments, the LB trough (Kibron MicrotroughX) was thoroughly cleaned with a number of solvents (acetone, dichloromethane, ethanol) and filled with Milli-Q water. Typically, 40 µL of rac-$Au_{38}(SC_2H_4Ph)_{24}$ nanocluster dissolved in 1 mg mL^{-1} solution of dichloromethane:*n*-hexane (70:30) was carefully spread on the water surface. After evaporation of the solvent, the barriers were slowly compressed (1 mm^2 s^{-1}) until the desired surface pressure. Vertically immersed substrate was retracted with a speed of 1 mm min^{-1}, while the barriers were being compressed to keep the surface pressure constant, unless stated otherwise. The pre-treatment of substrates involved cleaving of mica with a surgical knife and etching of silicon by reactive ion etching in CF_4 using March Stripper model CS-1701. Before the immersion in water, the substrates were thoroughly washed with chloroform, ethanol, and acetone. For high magnification TEM analysis, two S160 grids with a copper film and mesh 200 (Plano GmbH, Germany) were immersed vertically in water and separated after the retraction to ensure only one side of the TEM grid was covered with a film. The micrographs were obtained using CM200 Philips microscope operated at 200 kV. In LB experiments with long duration, it was ensured that the water surface was unchanged throughout the course of the experiment by carefully sealing the box surrounding the device.

AFM: Standard AC-mode AFM images in air were acquired with an MFP-3D bio Infinity microscope (Asylum Research, Oxford instruments, Santa Barbara, CA). AC240 TS (Asylum Research, Oxford instruments, Taiwan) cantilevers with nominal 7 nm tip radius and 1.7 N m^{-1} spring constant were used. Cantilevers were excited to free oscillation amplitudes (FOAs) of around 100 nm and the set points were ≈80% of the FOAs. Scan rate was typically 0.5 Hz. A Cypher AFM (Asylum Research, Oxford instruments, Santa Barbara, CA) was used to perform high-resolution AC-mode fast imaging in air. Images were acquired with Arrow-UHF cantilevers (Nano World, Switzerland) with nominal tip radius smaller than 10 nm, spring constant of around 6 N m^{-1}, and resonance frequency in air up to 2 MHz. Prior to each experiment, cantilever spring constant, resonance frequency, and optical sensitivity were determined using the GetRealTM automatic probe calibration routine included in the AFM software. Cantilevers were photo-thermally excited close to their resonance frequency with FOAs of around 10 nm and set points corresponding to 80% of the FOAs. High scan rates of around 10 Hz were used to minimize the effect of thermal drift. Typically, images of 100×100 nm^2 or 50×50 nm^2 with 256 points and lines were

acquired. To discriminate the obtained order from the typical AFM noise, only images that exhibited order of particles of the same size after immediate change of the size of the scan frame were considered. Gwyddion 2.56 was used for data visualization and analysis.[48]

XRR: Specular XRR and GIWAXS experiments were performed on a Xeuss 2.0 instrument (Xenocs, France) with a microfocused Cu k-alpha source (wavelength = 1.54 Å) and a Pilatus3 2-D detector (Dectris, Switzerland). The samples were firmly attached to the sample holder and the measurements were carried out in a horizontal configuration with two beam collimation slits (height x width), 0.5 × 1.2 mm and 0.3 × 1.2 mm, and a sample-detector distance = 1214 mm for XRR. For GIWAXS, the measurements were carried out at near-total reflection configuration, with beam collimation slits, 0.6 × 0.6 mm and 0.5 × 0.5 mm, and a sample-detector distance = 221 mm. In both cases, the sample area probed was of the order of several tens of mm^2. The total acquisition time per sample was about 3 h for XRR and about 15 h for GIWAXS.

The reflectivity curves were fitted with an n-layer model with the scattering length density normal to the interface $SLD(z)$ given in Equation (1)

$$\mathrm{SLD}(z) = \sum_{0}^{N}\left(\frac{\mathrm{SLD}_i - \mathrm{SLD}_{i+1}}{2}\right)\left(1 - erf\,\frac{(z - z_i)}{\sigma_i}\right) \quad (1)$$

where SLD_i and $(z_i - z_{i+1})$ are the scattering length density and the thickness of layer i, respectively, and σ_i is the interfacial roughness between layer i and i+1 described by an error function. $n = 0$ ($\mathrm{SLD}_0 = 0$) and $n = N$+1 ($\mathrm{SLD}_{N+1} \approx 24 \times 10^{-6}$ Å^{-2}) represent the two semi-infinite media, air and mica substrate, respectively. The best-fit set of parameters was determined by minimization of the $\chi 2$ parameter between the experimental and theoretical curve calculated using the classical optical matrix formalism.[49]

Supporting Information

Supporting Information is available from the Wiley Online Library or from the author.

Acknowledgements

Generous support by the University of Geneva and the Swiss National Science Foundation (grant number CRSII5_173720) is kindly acknowledged.

Conflict of Interest

The authors declare no conflict of interest.

Data Availability Statement

The data shown in the figures is available in Zenodo open-access repository at https://doi.org/10.5281/zenodo.4395978.

Keywords

clusters, films, gold, Langmuir–Blodgett technique, nanoclusters

Received: September 23, 2020
Revised: December 21, 2020
Published online:

[1] J. W. Boley, S.-H. Hyun, E. L. White, D. H. Thompson, R. K. Kramer, *ACS Appl. Mater. Interfaces* **2016**, *8*, 34171.
[2] M. Sainato, B. Shevitski, A. Sahu, J. D. Forster, S. Aloni, G. Barillaro, J. J. Urban, *ACS Omega* **2017**, *2*, 3681.
[3] K. Rajoua, L. Baklouti, F. Favier, *J. Phys. Chem. C* **2015**, *119*, 10130.
[4] Y. J. Kang, J. W. Oh, Y. R. Kim, J. S. Kim, H. Kim, *Chem. Commun.* **2010**, *46*, 5665.
[5] M.-C. Daniel, D. Astruc, *Chem. Rev.* **2004**, *104*, 293.
[6] P. D. Jadzinsky, G. Calero, C. J. Ackerson, D. A. Bushnell, R. D. Kornberg, *Science* **2007**, *318*, 430.
[7] A. Sels, G. Salassa, F. Cousin, L.-T. Lee, T. Bürgi, *Nanoscale* **2018**, *10*, 12754.
[8] T. Bürgi, *Nanoscale* **2015**, *7*, 15553.
[9] A. C. Templeton, W. P. Wuelfing, R. W. Murray, *Acc. Chem. Res.* **2000**, *33*, 27.
[10] H. Häkkinen, *Nat. Chem.* **2012**, *4*, 443.
[11] C. P. Collier, T. Vossmeyer, J. R. Heath, *Annu. Rev. Phys. Chem.* **1998**, *49*, 371.
[12] M. P. Pileni, *J. Phys. Chem. B* **2001**, *105*, 3358.
[13] J. Tang, G. Ge, L. E. Brus, *J. Phys. Chem. B* **2002**, *106*, 5653.
[14] C. Stowell, B. A. Korgel, *Nano Lett.* **2001**, *1*, 595.
[15] C. I. Yeo, J. H. Choi, J. B. Kim, J. C. Lee, Y. T. Lee, *Opt. Mater. Express* **2014**, *4*, 346.
[16] D.-S. Kim, N.-M. Hwang, *J. Phys. D: Appl. Phys.* **2018**, *51*, 463002.
[17] G. Schmid, N. Beyer, *Eur. J. Inorg. Chem.* **2000**, *2000*, 835.
[18] V. M. Raj Kumar Gupta, V. Manjuladevi, *Molecular Interactions at Interfaces*, InTech, Pilani, India **2012**.
[19] M. C. Petty, *Langmuir-Blodgett Films: An Introduction*, Cambridge University Press, Cambridge **1996**.
[20] F. P. Zamborini, M. C. Leopold, J. F. Hicks, P. J. Kulesza, M. A. Malik, R. W. Murray, *J. Am. Chem. Soc.* **2002**, *124*, 8958.
[21] A. Raveendran, M. V. Meli, *ACS Omega* **2017**, *2*, 4411.
[22] M. D. Phan, H. Kim, S. Lee, C.-J. Yu, B. Moon, K. Shin, *Langmuir* **2017**, *33*, 2590.
[23] R. M. Kenn, C. Boehm, A. M. Bibo, I. R. Peterson, H. Moehwald, J. Als-Nielsen, K. Kjaer, *J. Phys. Chem.* **1991**, *95*, 2092.
[24] M. C. Shih, T. M. Bohanon, J. M. Mikrut, P. Zschack, P. Dutta, *J. Chem. Phys.* **1992**, *96*, 1556.
[25] M. Lösche, H. P. Duwe, H. Möhwald, *J. Colloid Interface Sci.* **1988**, *126*, 432.
[26] O. N. Oliveira, C. Bonardi, *Langmuir* **1997**, *13*, 5920.
[27] Y. Tabe, T. Yamamoto, I. Nishiyama, K. M. Aoki, M. Yoneya, H. Yokoyama, *J. Phys. Chem. B* **2002**, *106*, 12089.
[28] G. H. Peters, S. Toxvaerd, N. B. Larsen, T. Bjørnholm, K. Schaumburg, K. Kjaer, *Nat. Struct. Biol.* **1995**, *2*, 395.
[29] M. Li, A. A. Acero, Z. Huang, S. A. Rice, *Nature* **1994**, *367*, 151.
[30] A. V. Tkachenko, Y. Rabin, *Phys. Rev. Lett.* **1996**, *76*, 2527.
[31] P. Chakraborty, A. Nag, A. Chakraborty, T. Pradeep, *Acc. Chem. Res.* **2019**, *52*, 2.
[32] K. R. Krishnadas, A. Ghosh, A. Baksi, I. Chakraborty, G. Natarajan, T. Pradeep, *J. Am. Chem. Soc.* **2016**, *138*, 140.
[33] K. R. Krishnadas, A. Baksi, A. Ghosh, G. Natarajan, T. Pradeep, *Nat. Commun.* **2016**, *7*, 13447.
[34] G. Schmid, O. Vidoni, V. Torma, K. Pollmeier, H. Rehage, A. Vassiliev, *Z. Anorg. Allg. Chem.* **2005**, *631*, 2792.
[35] J. J. Brown, J. A. Porter, C. P. Daghlian, U. J. Gibson, *Langmuir* **2001**, *17*, 7966.
[36] L. F. Chi, S. Rakers, M. Hartig, M. Gleiche, H. Fuchs, G. Schmid, *Colloids Surf., A* **2000**, *171*, 241.
[37] T. Yokoyama, N. Hirata, H. Tsunoyama, T. Eguchi, Y. Negishi, A. Nakajima, *J. Phys. Chem. C* **2020**, *124*, 363.
[38] H. Qian, W. T. Eckenhoff, Y. Zhu, T. Pintauer, R. Jin, *J. Am. Chem. Soc.* **2010**, *132*, 8280.
[39] A. Dhanabalan, L. Gaffo, A. M. Barros, W. C. Moreira, O. N. Oliveira, *Langmuir* **1999**, *15*, 3944.

[40] M. Fukuto, R. K. Heilmann, P. S. Pershan, A. Badia, R. B. Lennox, *J. Chem. Phys.* **2004**, *120*, 3446.
[41] S.-L. Xu, S.-Z. Kang, J. Lu, Y.-H. Liu, C. Wang, L.-J. Wan, C.-L. Bai, *Surf. Sci.* **2003**, *527*, L171.
[42] H. Tachibana, Y. Yamanaka, H. Sakai, M. Abe, M. Matsumoto, *J. Lumin.* **2000**, *87–89*, 800.
[43] X. M. Yang, D. Xiao, S. J. Xiao, Y. Wei, *Appl. Phys. A* **1994**, *59*, 139.
[44] Z. W. Wang, O. Toikkanen, B. M. Quinn, R. E. Palmer, *Small* **2011**, *7*, 1542.
[45] K. Vegso, P. Siffalovic, M. Jergel, M. Weis, M. Benkovicova, E. Majkova, S. Luby, T. Kocsis, I. Capek, *Langmuir* **2012**, *28*, 9395.
[46] D. G. Schultz, X.-M. Lin, D. Li, J. Gebhardt, M. Meron, J. Viccaro, B. Lin, *J. Phys. Chem. B* **2006**, *110*, 24522.
[47] H. Qian, Y. Zhu, R. Jin, *ACS Nano* **2009**, *3*, 3795.
[48] D. Nečas, P. Klapetek, *Cent. Eur. J. Phys.* **2011**, *10*, 181.
[49] M. Born, E. Wolf, *Principles of Optics: Electromagnetic Theory of Propagation, Interference and Diffraction of Light*, Cambridge University Press, Cambridge **1975**.